Supporting Information

Overall Water Splitting using Room-Temperature Synthesized NiFe Oxyfluoride Nanoporous Films

Kun Liang[1,#], Limin Guo[1,#], Kyle Marcus[1,2,#], Shoufeng Zhang[3,#], Zhenzhong Yang[4], Daniel E. Perea[5], Le Zhou[2], Yingge Du[4] & Yang Yang[1, 2,]*

[1]*NanoScience Technology Center, University of Central Florida, Orlando, FL 32826, USA.*

[2]*Department of Materials Science and Engineering, University of Central Florida, Orlando, FL 32826, USA.*

[3]*Laboratory of Theoretical and Computational Chemistry, Institute of Theoretical Chemistry, Jilin University, Changchun 130023, P.R. China*

[4]*Physical and Computational Sciences Directorate, Pacific Northwest National Laboratory, Richland, WA 99352, USA.*

[5]*Environmental Molecular Sciences Laboratory, Pacific Northwest National Laboratory, Richland, WA 99352, USA.*

[#]These authors contributed equally to this work.

[*]E-mail: Yang.Yang@ucf.edu

Focused Ion Beam (FIB) procedure and TEM images

A thin Pt layer was first deposited on the sample surface to protect the oxide layer. Two trenches were then cut on both sides of the Pt layer. A tungsten in-situ probe was tuned to touch the freed sample. Pt deposition was also used to adhere the probe to the sample, which was lifted out from the substrate and placed in a Cu grid for TEM observation. The specimen was then milled to about 100 nm for electron transparency.

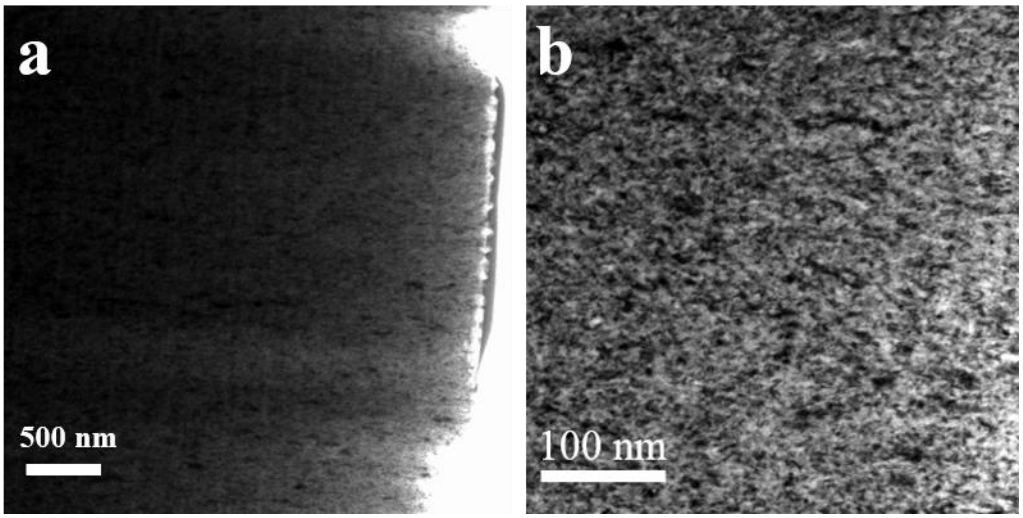

Figure S1. (a) TEM image after Focused Ion Beam (FIB) treatment. (b) TEM images of the holey film.

Atom Probe Tomography (APT)

Samples for APT analysis were prepared using an FEI Helios Nanolab Dual-Beam Focused Ion Beam/Scanning Electron Microscopy. A LEAP 4000X-HR atom probe equipped with a 355 nm UV picosecond pulsed laser from Cameca Instruments, Inc. was employed for APT analysis. The LEAP was operated with a laser pulsing frequency of 200 kHz, pulse energy of 20 pJ, and a detection rate of 0.01 ions per pulse, and a specimen base temperature of 44 K.

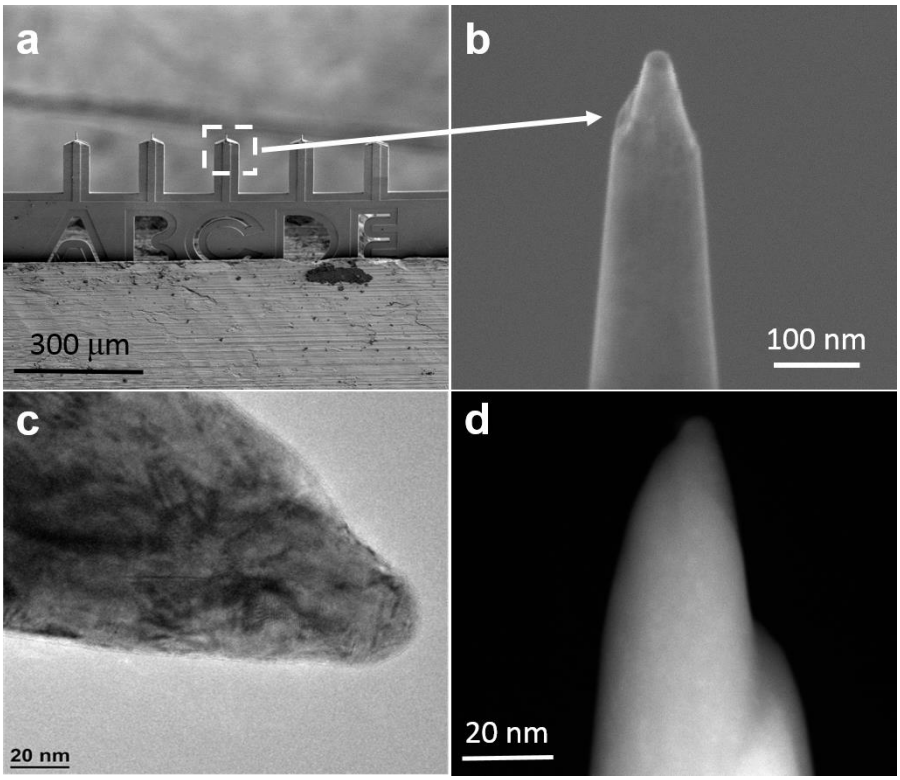

Figure S2. FIB preparation APT specimens for correlative analysis. (a-b) SEM images of the prepared specimens. (c-d) TEM and STEM images of the prepared specimen.

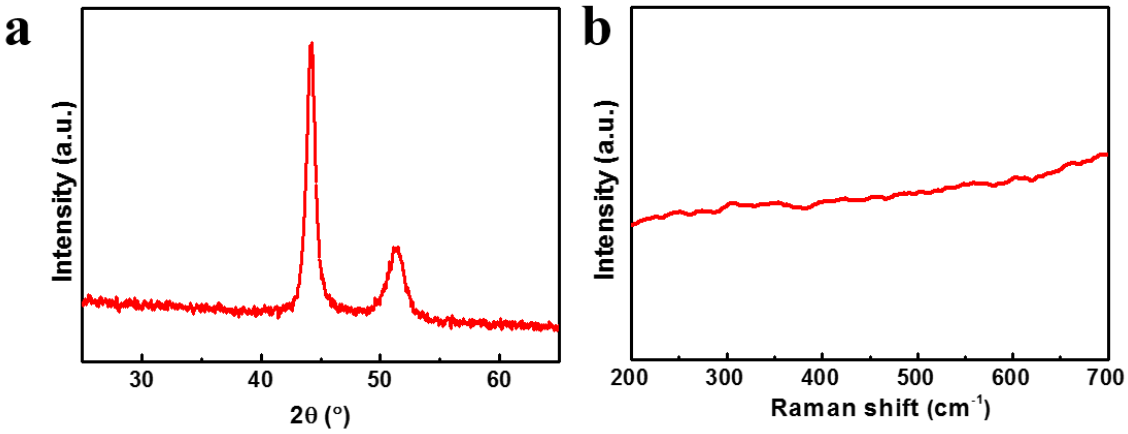

Figure S3. (a-b) XRD and Raman spectra of the NiFe oxyfluorides holey film.

XPS analysis

Fig. S4 shows the XPS spectra of the NiFeOF holey film with different Fe-contents. The spectra were calibrated using C 1s at 248.8 eV. Ni, Fe, O and F were detected from the holey film with different Fe-contents in the plating bath. The XPS Ni $2p_{3/2}$ peak at 857.1 eV with a satellite peak around 863.4 eV is ascribed to Ni^{2+}. The XPS Fe $2p_{3/2}$ peak at 712 eV is the typical energy of Fe^{3+} in Fe_2O_3. It is also not surprised to see the XPS F 1s peak from the holey film, which is commonly found in the anodized porous films using fluorine-containing (HF and NH_4F) electrolytes.

XPS depth profiles were performed with a 3 keV Ar^+ ion beam on a 2×2 mm^2 area and alternative mode in a total etching time of 25 min with an interval of 5 min. The spectra were fitted using a nonlinear least-square program with a mixed Gaussian-Lorentzian product function. The remarkable Ni 2p, Fe 2p, O 1s and F 1s peaks are exhibited in Figure S4b-e, respectively, to identify the chemical distribution of NiFeOF holey film from top to bottom. The Ni $2p_{3/2}$ peaks, as shown in Figure S4b, present Ni^{2+} peaks at the top layer, and Ni^{2+} and Ni (around 852.5 eV) are observed at the deeper layers.[1] As displayed in Figure S4c, the Fe 2p peaks just show Fe_2O_3 peak from the top to bottom. The O 1s peaks can be fitted to one peak corresponding to OH^- and another peak due to O^{2-}, which present different main peaks from the top to bottom, as shown in Figure S4d. The OH^-/O^{2-} ratio shows a sharp decrease from 2.0 (5 min) to 0.42 (20 min). Therefore, at the top layer, O 1s peaks from OH^- cover the main peak, which the main peak changes to O 1s peak from NiO at the deeper layers.[2] F 1s peaks keep stable from the top to bottom. The hydrated composition can improve wettability. The Ni phase becomes more prominent as observations deeper into the holey film interior, which can improve the conductivity and electrochemical performance.

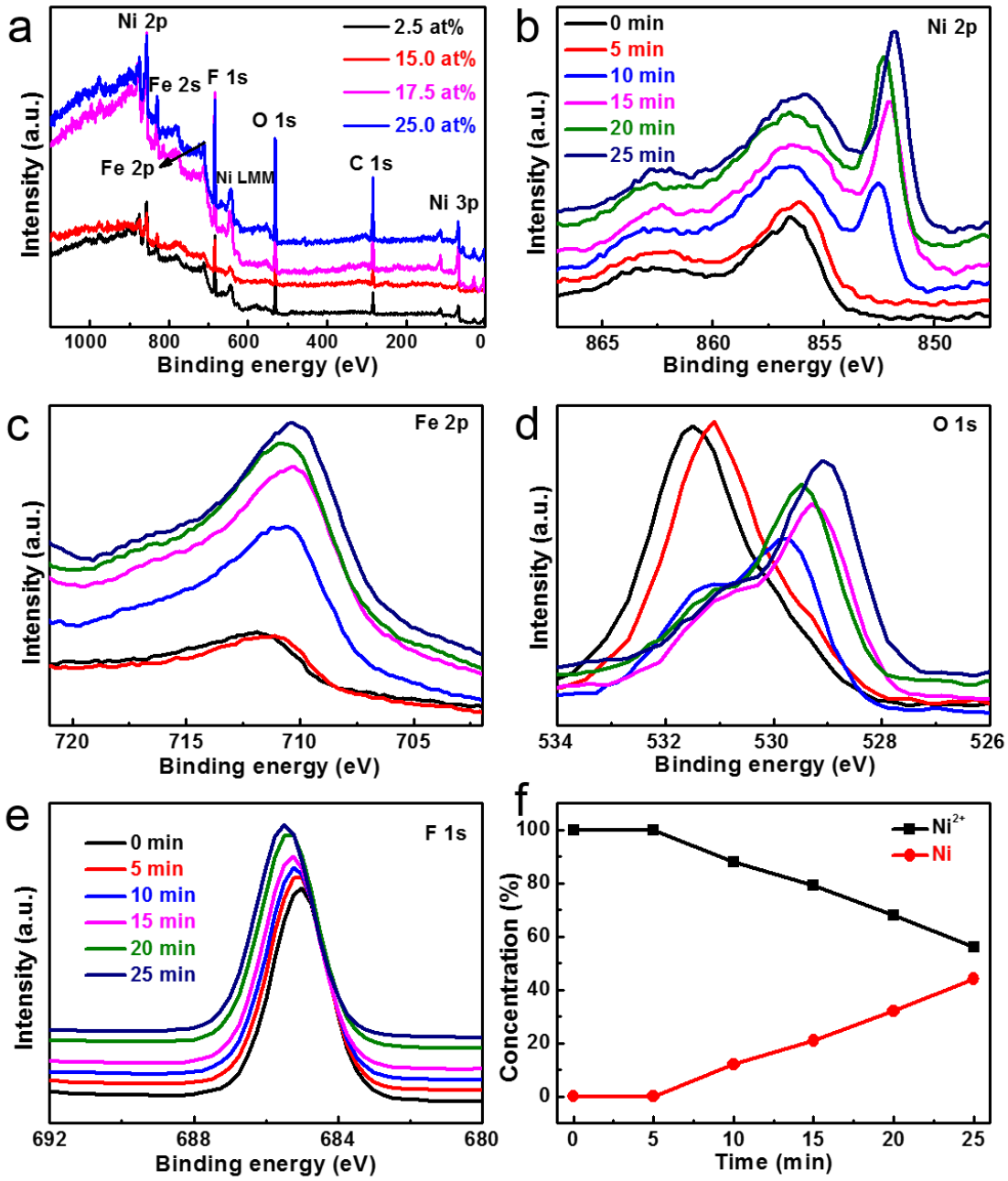

Figure S4. XPS depth profiles of the NiFe oxyfluorides holey film. (a) Survey scan spectrum. (b) Ni 2p peaks. (c) Fe 2p peaks. (d) O 1s peaks. (e) F 1s peaks. (f) The variations of Ni^{2+} and Ni derived from XPS depth profiles.

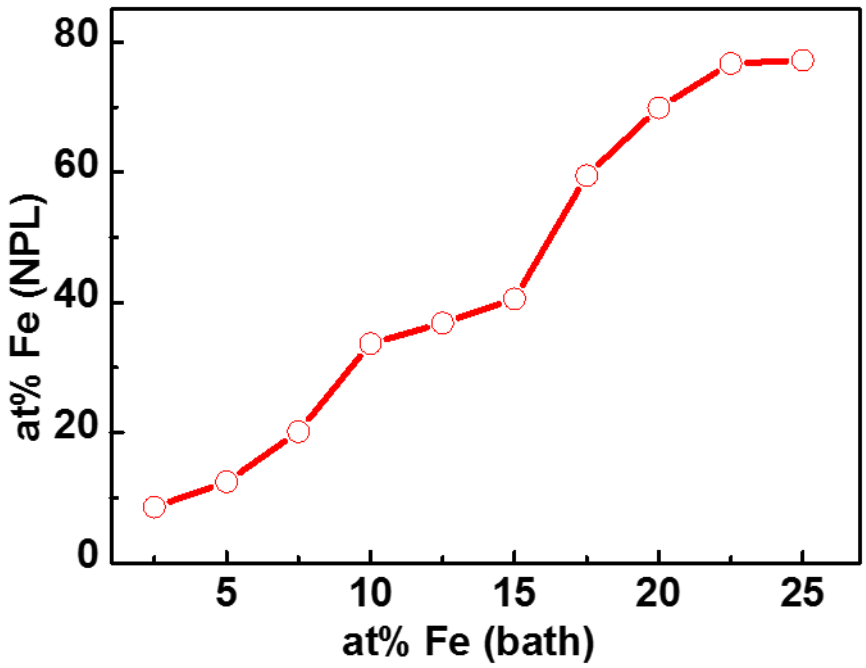

Figure S5. The variation of Fe-content in the oxyfluorides holey film with Fe-content in the bath.

Electrochemical active surface area and roughness factor (RF) of the holey film

The electrochemical active surface area (EASA) was determined from the electrochemical double layer capacitance (C_{DL}) of the holey film. The C_{DL} was estimated from cyclic voltammograms (CV) employed in a non-Faradaic region with different scan rates (v) from 10 to 100 mV s^{-1}. The C_{DL} can be calculated based on equation S1:

$$C_{DL} = \frac{i}{v} \qquad \text{(S1)}$$

where i is the double layer current from CV.

The EASA can be calculated from the equation S2:

$$\text{EASA} = \frac{C_{DL}}{C_s} \qquad \text{(S2)}$$

where C_s is the capacitance of an atomically smooth planar surface of the material per unit area. An average value of C_s = 40 μF cm^{-2} is used in this work.[4]

The RF is then calculated according to equation S3:

$$\text{RF} = \frac{\text{EASA}}{s} \qquad \text{(S3)}$$

where s is the geometric area of the holey film.[5]

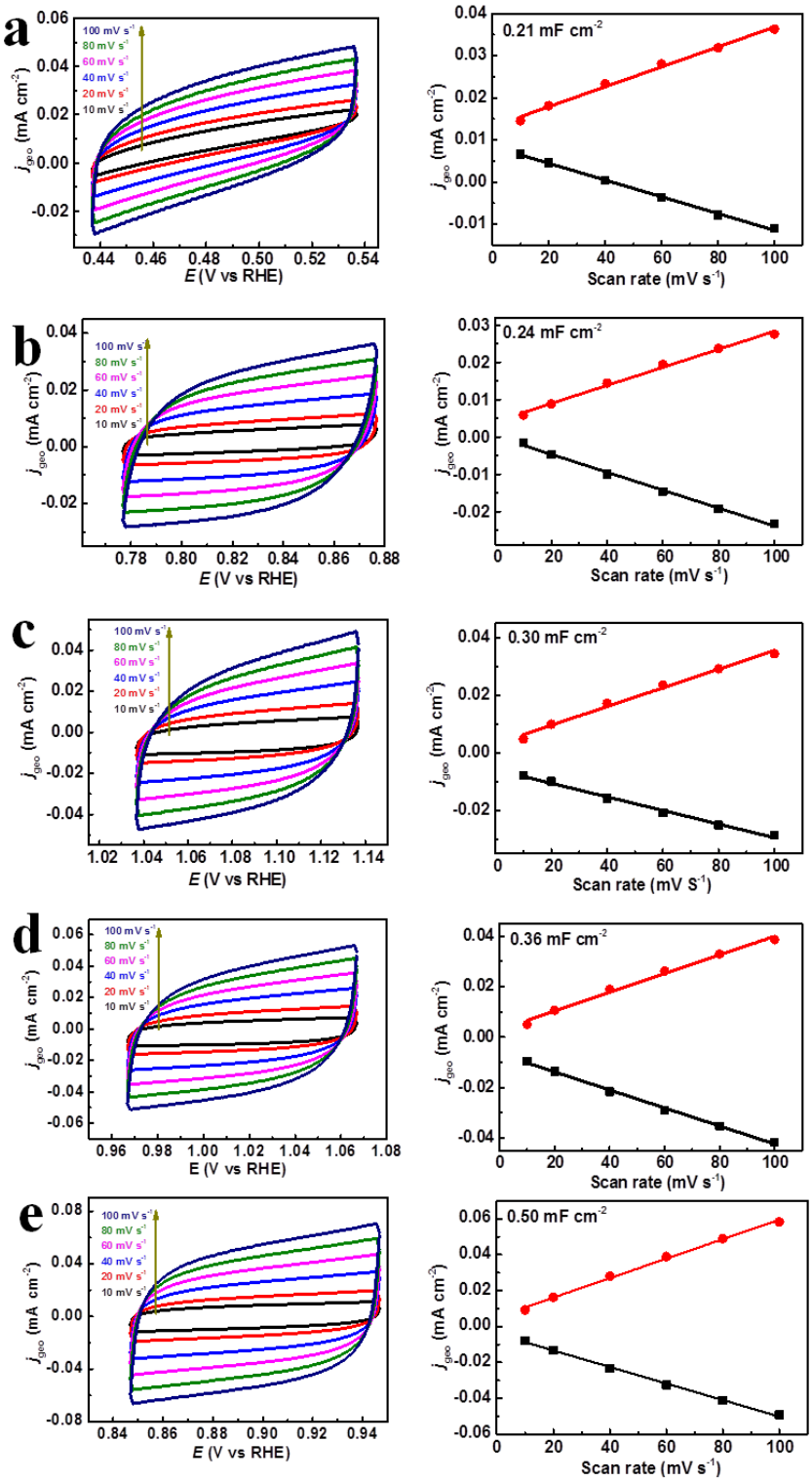
a
100 mV s-1
80 mV s-1
60 mV s-1
40 mV s-1
20 mV s-1
10 mV s-1
jgeo (mA cm-2)
E (V vs RHE)
0.21 mF cm-2
Scan rate (mV s-1)
b
0.24 mF cm-2
c
0.30 mF cm-2
d
E (V vs RHE)
0.36 mF cm-2
e
0.50 mF cm-2

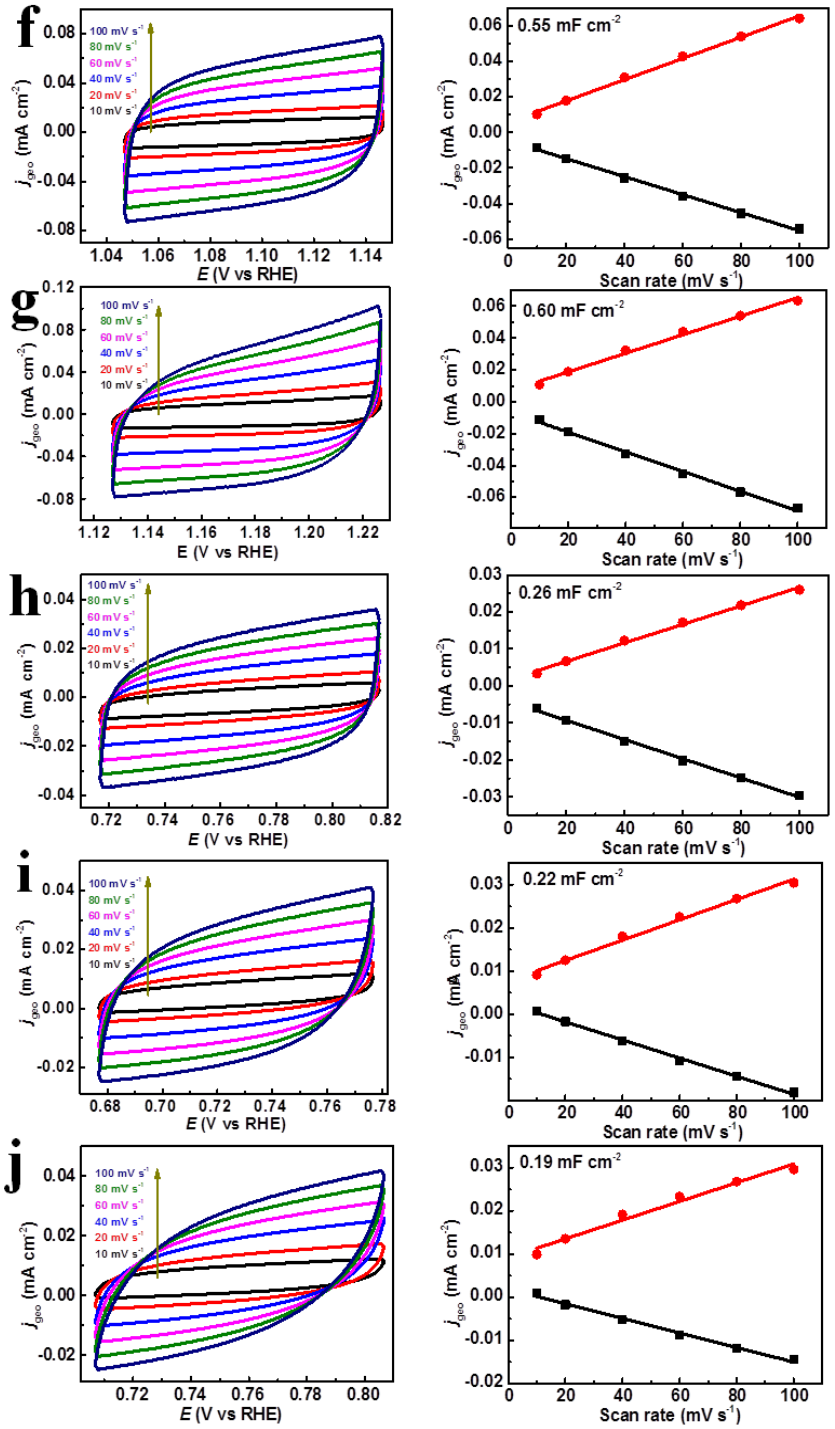

Figure S6. Electrochemical active surface area of the holey film. (a-j) CV curves and corresponding capacitance calculation with different Fe-contents in the bath.

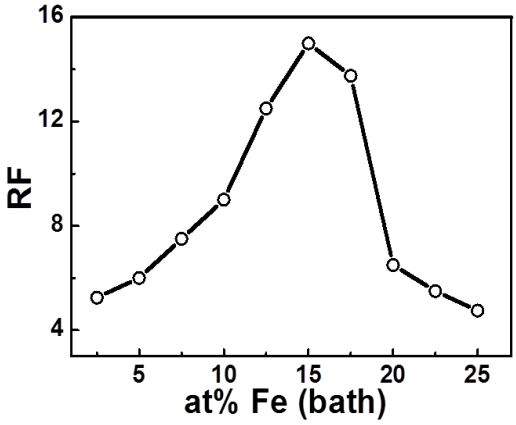

Figure S7. The variation of RF in the holey film with different Fe-contents.

Wettability and contact angle measurements of the holey film

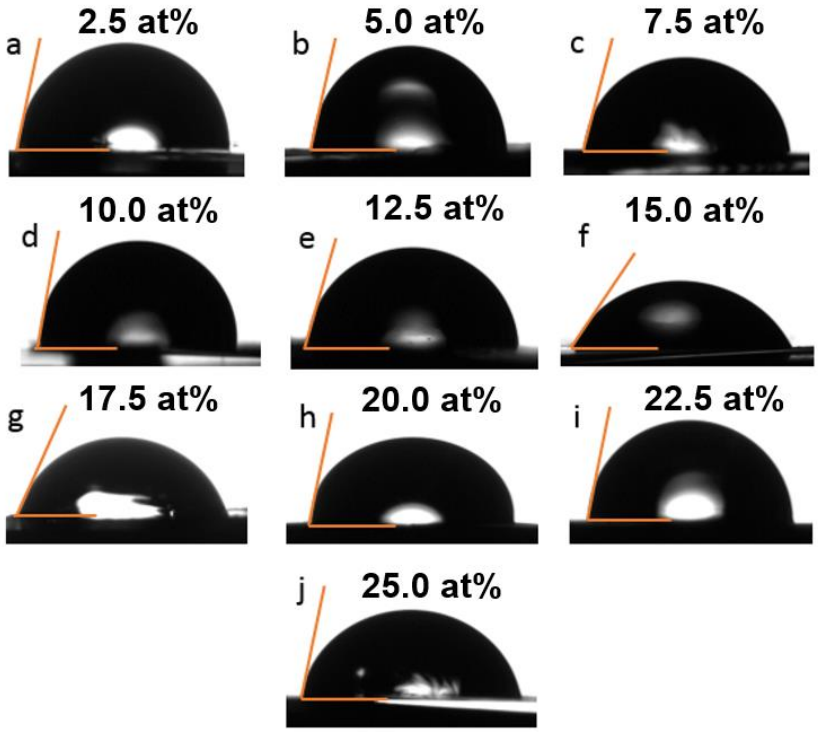

Figure S8. Contact angle measurements of the holey film with different Fe-contents.

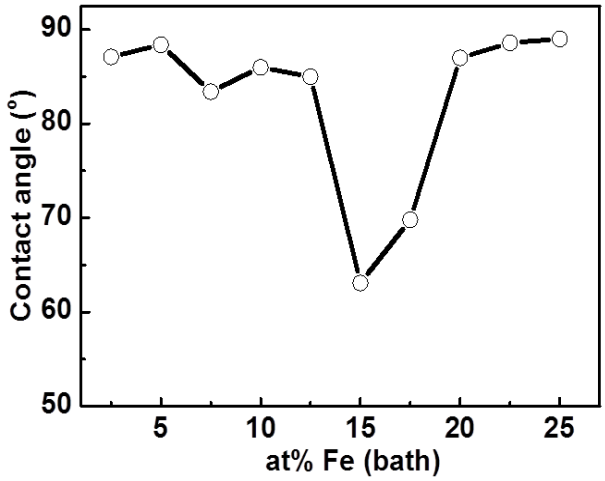

Figure S9. The variation of contact angles with different Fe-contents.

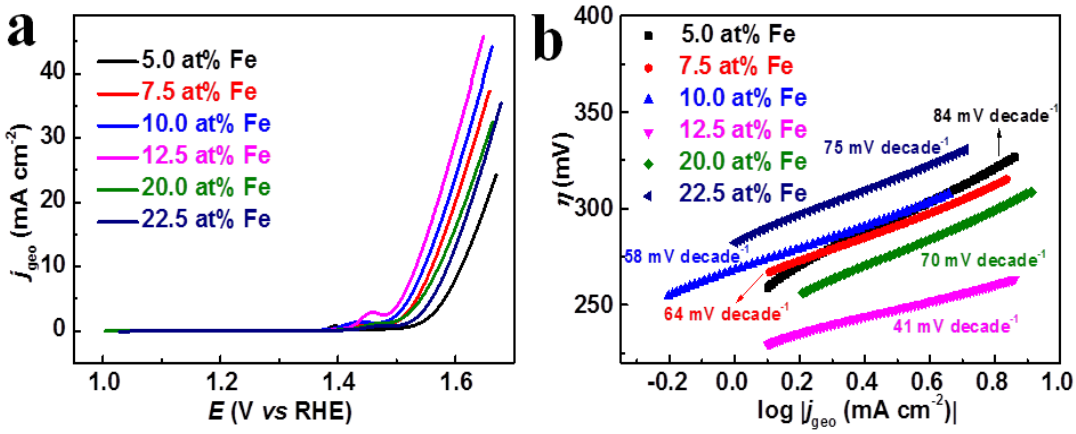

Figure S10. LSV and Tafel plots. (a-b) *iR*-corrected LSV curves and corresponding Tafel plots of the holey film with different Fe-contents for OER measured at 5 mV s^{-1} in 1 M NaOH aqueous solution.

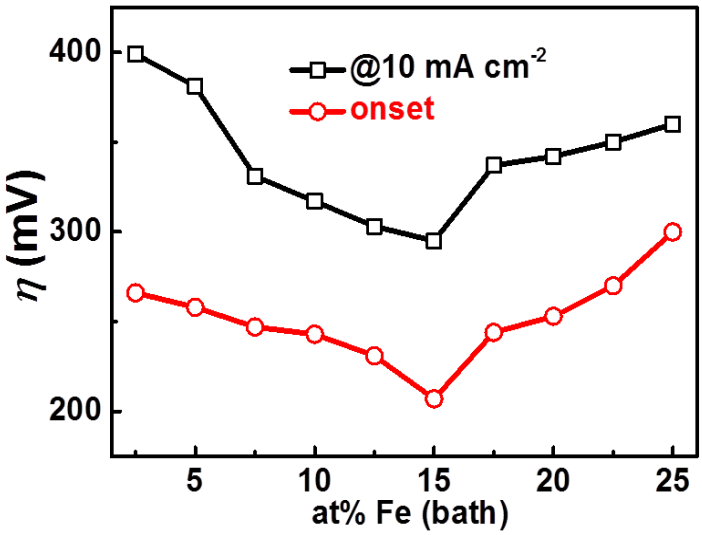

Figure S11. The variation of overpotential with Fe-contents in the holey film for OER.

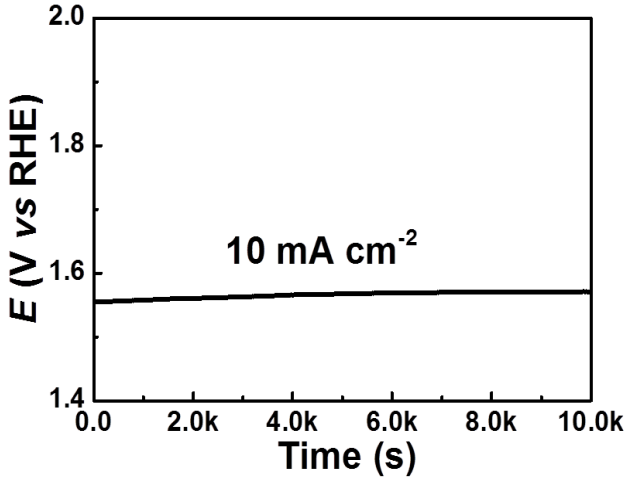

Figure S12. Chronopotentiometric test at a constant current density of 10 mA cm^{-2} for 10k seconds.

EIS analysis of the holey film for OER

Two semicircles were displayed in the Nyquist plots, revealing the presence of two time constants.[3] The first semicircle in the high-frequency region presents the charge transfer resistance (R_{ct1}) of surface metal oxides, which is related to the kinetics of water electrolysis.[4] The simulated R_{ct1} values for holey film display no apparent change around 3.5 Ω, implying fast charge transfer on the surface of the holey film. The low charge transfer resistance is mainly attributed to the high surface area and excellent conductivity. The excellent conductivity is enabled by the metallic framework remained in the holey film, suggesting an efficient pathway for electron transport throughout the entire thin-film electrode.[5] The second semicircle represent the charge transfer resistance (R_{ct2}) of inner oxide layers of the holey film, which varies with different Fe-content. One can see that the 15.0 at% of Fe-content exhibit the smallest semicircle in those holey films, which indicate the sample with 15.0 at% of Fe have a lower charge transfer impedance compared with others.[6]

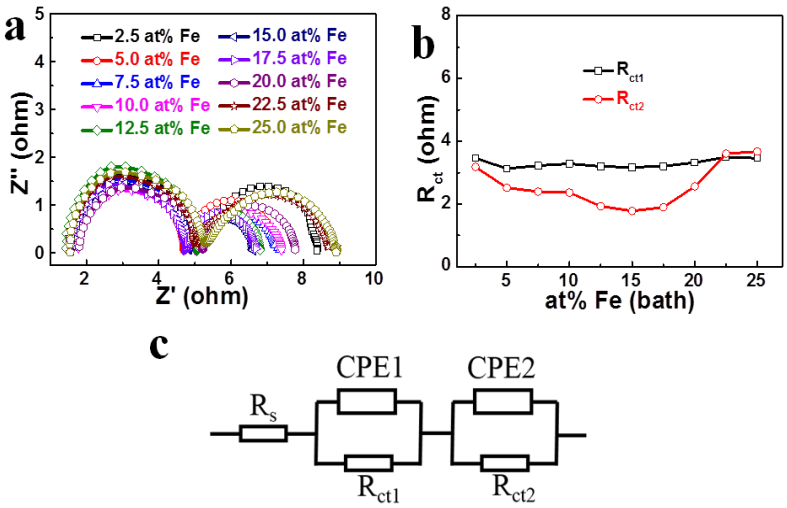

Figure S13. EIS test. (a) EIS analysis of the NiFeOF holey film with different Fe-contents measured at an overpotential of 350 mV. (b) The variation of the simulated charge transfer resistance with Fe-contents. (c) Equivalent electrical circuit used to simulate the OER process.

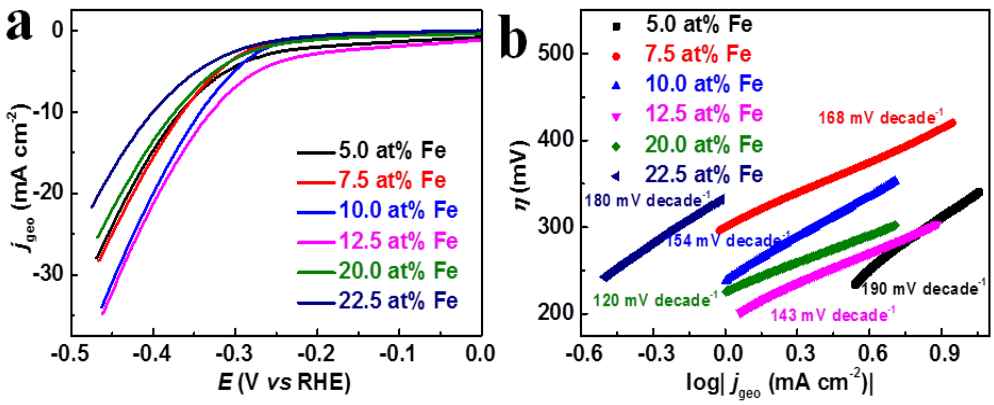

Figure S14. LSV and Tafel plots. (a-b) *iR*-corrected LSV curves and corresponding Tafel plots of the holey film for HER measured at 5 mV s^{-1} in 1 M NaOH aqueous solution.

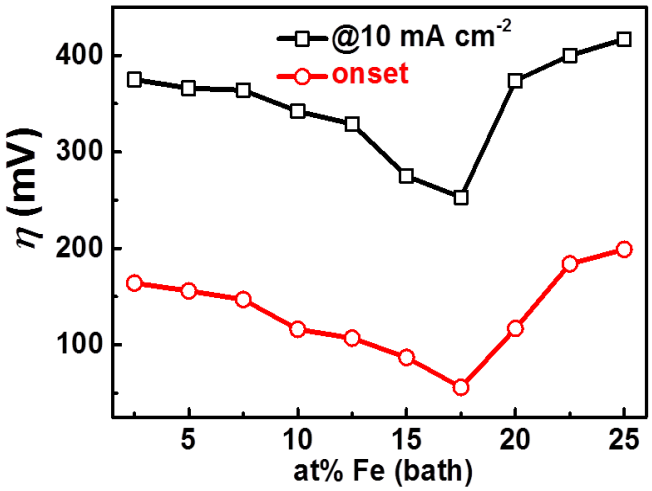

Figure S15. The variation of overpotential in the holey film with different Fe-contents for HER.

EIS analysis of the holey film for HER

To investigate the HER kinetics, the EIS was performed from 100 kHz to 0.01 Hz at an overpotential of 150 mV. As shown in Fig S16a, the two semicircles of the Nyquist plot represent two constants impedance of the holey film for HER. A parallel equivalent circuit model was then employed to fit the Nyquist plot. The first semicircle in the high-frequency region is related to the charge transfer resistance (R_{ct1}) of surface oxide layers.[7] The simulated values for R_{ct1} is about 4 Ω, implying the similar kinetics and the fast charge transfer process occured on the surface of all holey film samples for hydrogen evolution.[8] The second semicircle represent the charge transfer resistance (R_{ct2}) of inner oxide layers of the holey film, which varies markedly with different Fe-content. This indicates that the inner conductivity of holey film is determined by the Fe-content, especially the 17.5 at% of Fe-content is more benefit for the charge transfer than others.

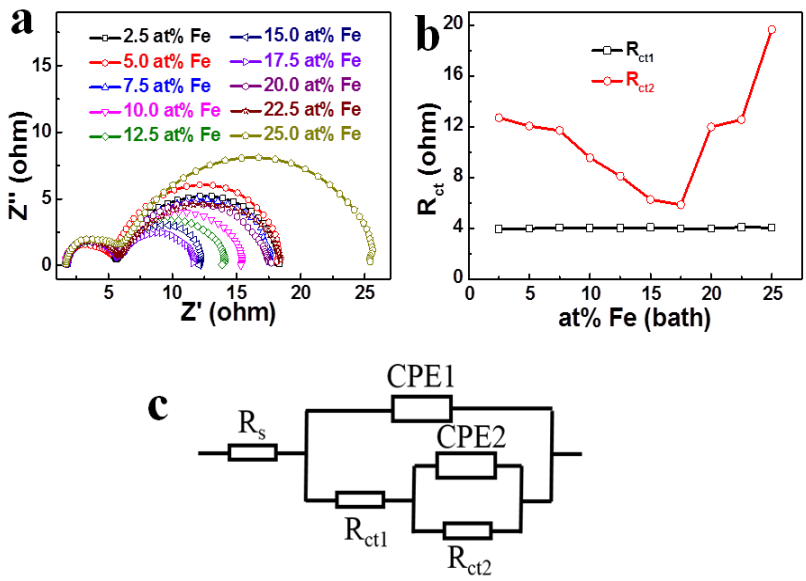

Figure S16. EIS test. (a) EIS analysis of the NiFeOF holey film with different Fe-contents measured at an overpotential of 150 mV. (b) The variation of charge transfer resistance with Fe-contents. (c) Equivalent electrical circuit used to simulate the HER process.

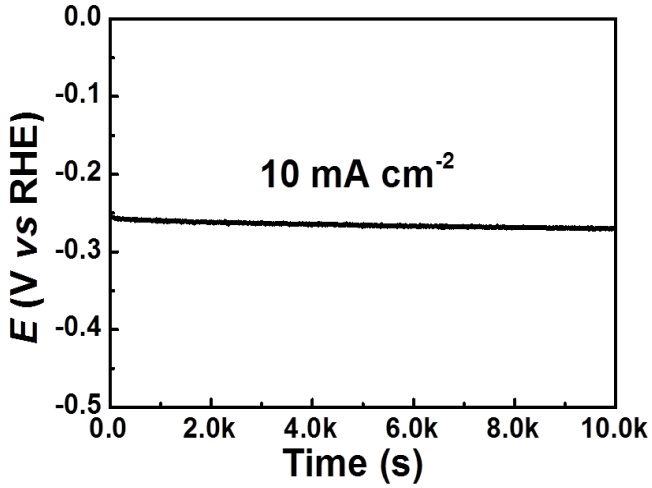

Figure S17. Chronopotentiometric test at a constant current density of 10 mA cm^{-2} for 10k seconds.

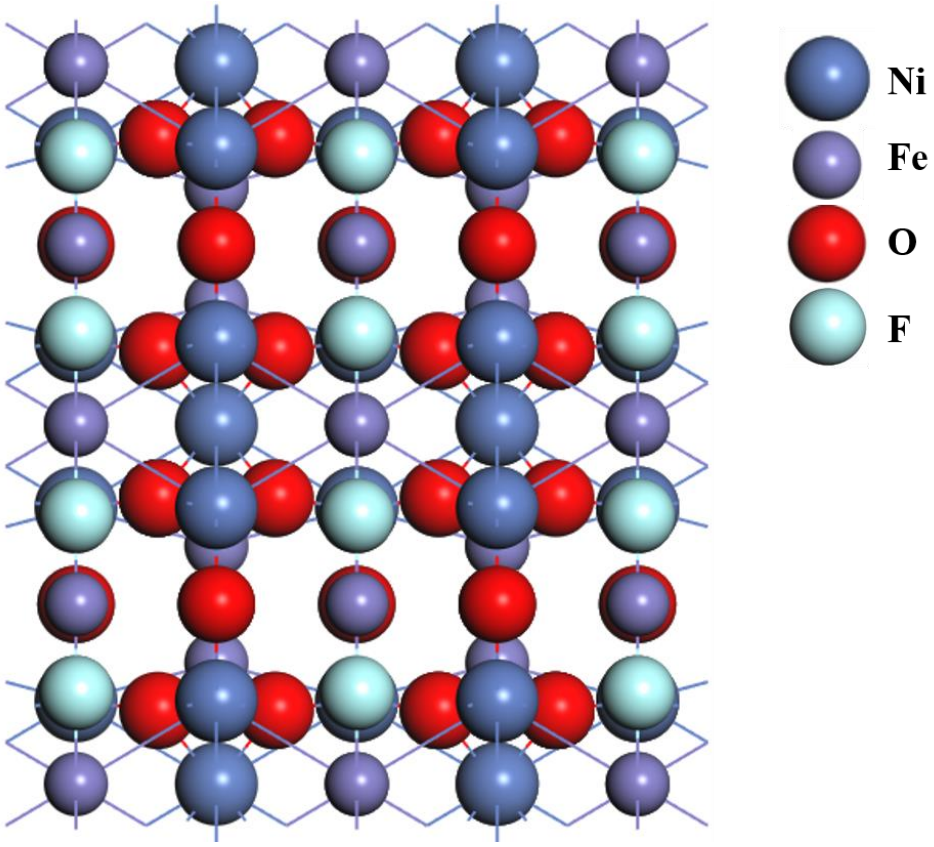

Figure S18. Simulated structure of NiFeOF.

Table S1. Comparison with other OER catalysts.

Catalysts	Tafel slope (mV decade^{-1})	Overpotential at 10 mA cm^{-2} (mV)	Electrolyte	Reference
15 at% Fe holey film	**38**	**295**	**1 M NaOH**	**This work**
10 at% Co NPL	44	325	1 M NaOH	6
40 at% Co NPL	39	333	1 M NaOH	6
CQD/NiFe-LDH	35	305	0.1 M KOH	9
α-$Ni(OH)_2$ nanocrystals	42	331	0.1 M KOH	4
NiFe LDH	67	350	1 M KOH	10
NiCo LDH	65	390	1 M KOH	10
IrO_2/C	---	310	0.1 M KOH	11
NiO	65	365	1 M KOH	12
m-NiFe/CNx	59.1	470	0.1 M KOH	13
NiFe oxide nanotube array	---	142	0.1 M KOH	14
Porous NiFe oxide	42	328	0.1 M KOH	15
Dendritic NiFe film	---	440	1 M NaOH	16
nNiFe LDH/HGF	45	337	0.1 M KOH	3
Ni_2P/Ni/NF	--	200	1 M KOH	17
Co-P	47	345	1 M KOH	18
h-NiS_x	96	180	1 M KOH	19

Table S2. Comparison with other HER catalysts.

Catalysts	Tafel slope (mV decade^{-1})	Overpotential at 10 mA cm^{-2} (mV)	Electrolyte	Reference
17.5 at% Fe holey film	**96**	**253**	**1 M NaOH**	**This work**
Ni_2P	---	220	1 M KOH	12
Ni_2P/Ni/NF	72	98	1 M KOH	17
Co-P	42	94	1 M KOH	18
h-NiS_x	99	60	1 M KOH	19
CoOx@AC	---	270	1 M KOH	20
CoP/CC	129	209	1 M KOH	21
$NiCo_2S_4$/CC	141	---	1 M KOH	22
$NiCo_2O_4$/CC	207	---	1 M KOH	22
NiSe/NF	120	---	1 M KOH	23

Reference

[1] Bhosale, R.; Kelkar, S.; Parte, G.; Fernandes, R.; Kothari, D.; Ogale, S. *ACS Appl. Mater. Interfaces* **2015**, *7*, 20053.

[2] Kim, J. Y.; Jang, J. W.; Youn, D. H.; Magesh, G.; Lee, J. S. *Adv. Energy Mater.* **2014**, *4*, 1400476.

[3] Tang, C.; Wang, H. S.; Wang, H. F.; Zhang, Q.; Tian, G. L.; Nie, J. Q.; Wei, F. *Adv. mater.* **2015,** 27, 4516.

[4] Gao, M.; Sheng, W.; Zhuang, Z.; Fang, Q.; Gu, S.; Jiang, J.; Yan, Y. *J. Am. Chem. Soc.* **2014**, *136*, 7077.

[5] Tian, G. L.; Zhang, Q.; Zhang, B.; Jin, Y. G.; Huang, J. Q.; Su, D. S.; Wei, F. *Adv. Funct. Mater.* **2014,** *24*, 5956.

[6] Yang, Y.; Fei, H.; Ruan, G.; Xiang, C.; Tour, J. M. *ACS Nano* **2014**, *8*, 9518.

[7] Damian, A.; Omanovic, S. *J. Power Sources* **2006,** *158*, 464.

[8] Zhang, Y.; Ouyang, B.; Xu, J.; Chen, S.; Rawat, R. S.; Fan, H. J. *Adv. Energy Mater.* **2016,** *6*, 1600221.

[9] Tang, D.; Liu, J.; Wu, X.; Liu, R.; Han, X.; Han, Y.; Huang, H.; Liu, Y.; Kang, Z. *ACS Appl. Mater. Interfaces* **2014**, *6*, 7918.

[10] Song, F.; Hu, X. *Nat. Commun.* **2014**, *5*, 4477.

[11] Zhao, Y.; Nakamura, R.; Kamiya, K.; Nakanishi, S.; Hashimoto, K. *Nat. Commun.* **2013**, *4*, 2390.

[12] Stern, L. A.; Feng, L.; Song, F.; Hu, X. *Energy Environ. Sci.* **2015**, *8*, 2347.

[13] Ci, S.; Mao, S.; Hou, Y.; Cui, S.; Kim, H.; Ren, R.; Wen, Z.; Chen, J. *J. Mater. Chem. A* **2015**, *3*, 7986.

[14] Zhao, Z.; Wu, H.; He, H.; Xu, X.; Jin, Y. *J. Mater. Chem. A* **2015**, *3*, 7179.

[15] Qi, J.; Zhang, W.; Xiang, R.; Liu, K.; Wang, H. Y.; Chen, M.; Han, Y.; Cao, R. *Adv. Sci.* **2015**, *2*, 1500199.

[16] Kim, K. H.; Zheng, J. Y.; Shin, W.; Kang, Y. S. *RSC Adv.* **2012**, *2*, 4759.

[17] You, B.; Jiang, N.; Sheng, M.; Bhushan, M. W.; Sun, Y. *ACS Catal*. **2016**, *6*, 714-721.

[18] Jiang, N.; You, B.; Sheng, M.; Sun, Y. *Angew. Chem.* **2015**, *127*, 6349-6352.

[19] You, B.; Sun, Y. *Adv. Energy Mater.* **2016**, *6*, 1502333.

[20] Jin, H.; Wang, J.; Su, D.; Wei, Z.; Pang, Z.; Wang, Y. *J. Am. Chem. Soc.* **2015**, *137*, 2688.

[21] Tian, J.; Liu, Q.; Asiri, A. M.; Sun, X. *J. Am. Chem. Soc.* **2014**, *136*, 7587.

[22] Liu, D.; Lu, Q.; Luo, Y.; Sun, X.; Asiri, A. M. *Nanoscale* **2015**, *7*, 15122.

[23] Tang, C.; Cheng, N.; Pu, Z.; Xing, W.; Sun, X. *Angew. Chem.* **2015**, *54*, 9483.